RSC Advances

PAPER

View Article Online
View Journal | View Issue

Cite this: *RSC Adv.*, 2026, **16**, 409

Synthesis, characterization, and anticancer potential of novel NHC ligands and their selenium complexes: a combined *in vitro* and *in silico* investigation

Boutheina Boualia,[ab] Abd el-Krim Sandeli,[c] Enes Evren,[b] İsmail Özdemir,[bd] Hüseyin Karci,[b] Muhammed Dündar,[e] İlknur Özdemir,[bd] Nevin Gürbüz,[bd] Ahmet Koç[f] and Houssem Boulebd[*g]

We report herein the efficient synthesis of new benzimidazolium salts (**A1–A6**) and their corresponding selenium-NHC complexes (**B1–B6**), along with the evaluation of their cytotoxicity profiles against two cancer cell lines (HCT116 and SH-SY5Y) and one normal cell line (BEAS-2B). The findings revealed that the benzimidazolium salts (**A1–A6**) exhibited significantly higher cytotoxicity toward all tested cell lines compared to their selenium derivatives (**B1–B6**). Among them, compounds **A3**, **A4**, and **A5** showed the most potent cytotoxic effects, with IC_{50} values ranging from 3.09 to 26.12 μM, approximately ten times lower than that of cisplatin. However, these compounds also exhibited relatively low IC_{50} values in normal BEAS-2B cells, although still higher than those observed in the cancer cell lines, indicating a preferential cytotoxicity toward cancer cells. Structure–activity relationship analysis revealed that the benzimidazolium core acts as the pharmacophore of these compounds, while substitution on the aromatic ring—particularly with bulky groups—enhances cytotoxicity. Conversely, incorporation of the selenium atom was found to markedly reduce or even eliminate cytotoxicity up to concentrations of 800 μM. Further *in silico* studies were conducted to gain a deeper understanding of the molecular structures and chemical reactivity of these compounds. In addition, molecular docking studies against PARP-1 and tubulin highlighted the strong inhibitory potential of the most active compounds (**A3**, **A4**, and **A5**) toward both targets, suggesting their potential involvement in the observed cytotoxic effects. Overall, these investigations propose benzimidazolium salts **A3**, **A4**, and **A5** as promising anticancer agents and highlight the selenium derivatives as non-toxic selenium-based NHC complexes. Further studies should be undertaken to optimize the biological activity of these compounds and to enhance their selectivity toward cancer cells.

Received 31st October 2025
Accepted 12th December 2025

DOI: 10.1039/d5ra08393a

rsc.li/rsc-advances

1. Introduction

Cancer remains a leading cause of morbidity and mortality worldwide, necessitating the continued development of novel therapeutic agents with improved efficacy and selectivity. The identification of cisplatin's anticancer properties by Rosenberg[1] led to metal-based compounds becoming a major focus in anticancer drug development. Since then, the search for novel metal-based therapeutics has intensified. However, despite their success, platinum-based drugs such as cisplatin suffer from severe side effects, limited selectivity toward malignant cells, and the emergence of resistance.[2] These challenges have stimulated extensive efforts to design and evaluate new classes of inorganic and organometallic compounds with improved therapeutic profiles.[3–5] During recent decades, numerous inorganic species and organometallic compounds have been synthesized and assessed for their antitumor activity, including those based on ruthenium, iron, palladium, silver, and gold.[6–8] Unlike platinum complexes, which primarily act by binding to DNA, many of these compounds exert their biological effects through alternative mechanisms, such as the inhibition of

[a]*The Molecular and Structural Environmental Chemistry Research Unit, Faculty of Exact Sciences, Brother's Mentouri Constantine 1 University, Constantine, Algeria*
[b]*İnönü University Drug Administration and Research Center, 44280-Malatya, Turkey*
[c]*Pharmaceutical Sciences Research Center (CRSP), Constantine 25000, Algeria*
[d]*İnönü University, Faculty of Arts and Sciences, Department of Chemistry, 44280-Malatya, Turkey*
[e]*Inönü University, Faculty of Arts and Sciences, Department of Molecular Biology and Genetics, 44280-Malatya, Turkey*
[f]*İnönü University, Faculty of Medicine, Department of Medical Genetics, 44280-Malatya, Turkey*
[g]*Laboratory of Synthesis of Molecules with Biological Interest, Frères Mentouri Constantine 1 University, Constantine 25017, Algeria. E-mail: boulebd.houssem@umc.edu.dz*

overexpressed enzymes or the modulation of dysregulated cellular pathways in cancer cells.[9] These findings have broadened the scope of metal-based drug design beyond DNA targeting.

In this context, selenium-based N-heterocyclic carbene (NHC) ligands have attracted growing interest due to the complementary advantages offered by both NHC frameworks and selenium.[10,11] NHC ligands are known for their strong σ-donating properties, structural tunability stability,[12,13] and for their chemopreventive and cytotoxic properties, while selenium plays an essential role in redox homeostasis and cellular signalling, and exhibits pro-apoptotic and cytotoxic activities.[14,15] The combination of these features in selenium-NHC complexes offers a promising strategy for designing multifunctional anticancer agents capable of interacting with diverse biological targets.[16] NHCs, particularly those derived from benzimidazolium salts, have garnered significant attention in recent years due to their structural versatility, thermal stability, and promising bioactivity.[17] Several studies have highlighted the potential of NHCs as pharmacophores with anticancer, antimicrobial, and enzyme inhibitory properties.[18] Moreover, NHCs serve as excellent ligands for metal and metalloid coordination, enabling the formation of biologically active complexes.[19]

In light of the growing biological relevance of NHC ligands and as a continuation of our previous studies on biologically active metal–organic compounds derived from NHC systems,[20,21] the present work was designed to further explore their therapeutic potential. In this context, a new series of benzimidazolium-based NHC ligands was synthesized together with their corresponding NHC-selenium adducts. The incorporation of selenium was hypothesized to enhance biological efficacy through synergistic effects, potentially improving cytotoxic activity against cancer cells while maintaining or enhancing selectivity toward non-cancerous cells. The anticancer potential of the synthesized compounds was evaluated *in vitro* using the MTT assay against three human cell lines: HCT116 (colon cancer), SH-SY5Y (neuroblastoma), and BEAS-2B (non-cancerous lung epithelial). A comparative analysis was conducted to assess the cytotoxic performance of the ligands relative to their selenium complexes. Furthermore, molecular docking studies were carried out to investigate the binding interactions of the most active compounds with biologically relevant targets, providing insights into their possible mechanisms of action.

2. Experimental section

2.1. Chemistry

2.1.1. General information. All experiments and analyses were performed at the İnönü University Drug Administration and Research Center, including synthesis, purification, and compound characterization. All reagents and solvents used in the synthesis were of analytical or reagent grade and were used without further purification unless otherwise specified. The chemicals were purchased from Merck, Sigma-Aldrich, and Fluka, ensuring the reproducibility and reliability of the experimental results. All reactions were conducted in oven-dried glassware under a nitrogen atmosphere, and progress was monitored by thin-layer chromatography (TLC) when applicable. Purification of crude products was carried out by recrystallization or flash column chromatography on silica gel using suitable solvent systems. Nuclear Magnetic Resonance (NMR) spectroscopy was used for structural elucidation. ^{1}H NMR and ^{13}C NMR spectra were recorded on a Varian as 400 Merkur spectrometer operating at 400 MHz (^{1}H) and 100 MHz (^{13}C), using $CDCl_3$ or DMSO-d_6 as solvents and tetramethylsilane (TMS) as the internal standard. Fourier Transform Infrared (FT-IR) spectra were recorded on a PerkinElmer Spectrum 100 spectrometer using the ATR unit in the range of 400–4000 cm^{-1}. Melting points were determined using a Kofler-type WME melting point apparatus (Scientific Apparatus for Research and Industry Laboratory Equipment, Model No. 6809, 230 V, 0.44 A, 100 W). Mass spectrometric analysis was performed to determine the molecular weights and fragmentation patterns of the synthesized compounds.

2.1.2. General procedure for the synthesis of NHC ligands (A1–A6). Benzimidazolium salts-derived NHC Ligands were synthesized *via* a modified procedure based on previously reported methods.[22] In a typical reaction, 1-cyclopentyl-1*H*-benzo[*d*]imidazole (1.0 equiv.) and the corresponding alkyl halide (1.0 equiv.) were dissolved in dimethylformamide (DMF) and stirred at 90 °C under a nitrogen atmosphere for 48 hours. After completion of the reaction, the solvent was removed under vacuum. The residue was treated with diethyl ether (50 mL) to precipitate the product as a solid, which was then collected by filtration. The crude material was washed with cold diethyl ether (3 × 20 mL) and dried under reduced pressure. Recrystallization of the resulting solid from a dichloromethane/diethyl ether mixture (1 : 3, v/v) at room temperature afforded the pure benzimidazolium salts, which were stored in a desiccator until further use.

*2.1.2.1 3-Cyclopentyl-5,6-dimethyl-1-(4-methylbenzyl)-1H-benzo[d]imidazole-3-ium chloride (**A1**).* Yield 76% (540 mg, white solid); m.p. = 174 °C; FT-IR ν(C–N) = 1550 cm^{-1}. ^{1}H NMR (400 MHz, DMSO-d^6, TMS, 298 K): δ (ppm) = 10.33 (s, 1H, NC*H*N); 7.87 (s, 1H, Ar); 7.71 (s, 1H, Ar); 7.44 (d, J = 8.2 Hz, 2H, Ar); 7.20 (s, 2H, Ar); 5.69 (s, 2H, N–CH_2); 5.10 (s, 1H, N–C*H*–(CH_2)); 2.39 (s, 3H, CH_3–Ph); 2.35 (s, 6H, 2CH_3(benzimidazole)); 2.26 (m, 2H, N–CH–CH_2); 2.06 (m, 2H, N–CH–CH_2); 1.91 (m, 2H, CH–CH_2–CH_2); 1.75 (m, 2H, CH–CH_2–CH_2). ^{13}C NMR (100 MHz, DMSO-d^6, TMS, 298): δ (ppm) = 140.2 (N*C*HN); 138.4 (C, CH_3–*C*q); 136.8 (C, CH_3–*C*q); 136.7 (C, CH_3–*C*q); 131.9 (C, Cq); 130.2 (C, Cq); 129.9 (C, Cq); 129.8 (2C, **Ar**); 128.5 (2C, **Ar**); 114.2 (C, *C*H); 113.7 (C, *C*H); 59.3 (C, N–*C*H_2); 49.9 (C, N–*C*H); 32.0 (2C, CH_2–N–CH_2); 23.7 (2C, CH_2–N–CH_2); 21.1 (1C, CH_3); 20.4 (1C, CH_3); 20.4 (1C, CH_3). $C_{22}H_{27}ClN_2$ (M_w = 354.91 g mol^{-1}) HRMS (ESI) ($C_{22}H_{27}N_2^+$) m/z calcd $[M + H]^+$ 319.2174, found 319.2150.

*2.1.2.2 3-Cyclopentyl-1-(3,5-dimethylbenzyl)-5,6-dimethyl-1H-benzo[d]imidazole-3-ium bromide (**A2**).* Yield 78% (652 mg, white solid); m.p. = 202 °C; FT-IR ν(C–N) = 1550 cm^{-1}. ^{1}H NMR (400 MHz, DMSO-d^6, TMS, 298 K): δ (ppm) = 10.02 (s, 1H, NC*H*N); 7.70 (s, 1H, Ar); 7.61 (s, 1H, Ar); 7.11 (s, 2H, Ar); 6.97 (s, H, Ar); 5.66 (s, 1H, CH_2–C*H*–CH_2); 5.61 (s, 2H, N–CH_2); 2.40 (s, 3H, CH_3(benzimidazole)); 2.36 (s, 3H, CH_3(benzimidazole)); 2.24 (s,

6H, 2CH_3(benzyl)); 2.24 (m, 2H, N–CH–CH_2); 2.05 (m, 2H, N–CH–CH_2); 1.90 (m, 2H, CH–CH$_2$–CH_2); 1.77 (m, 2H, CH–CH$_2$–CH_2). ^{13}C NMR (100 MHz, DMSO-d^6, TMS, 298 K): δ (ppm) = 140.2 (NCHN); 138.6 (Cq, CH$_3$–Cq); 138.5 (Cq, CH$_3$–Cq); 136.9 (C, CH$_3$–Cq); 136.8 (C, CH$_3$–Cq); 134.6 (C, Cq); 130.4 (C, Cq); 130.2 (C, Cq); 130.1 (C, Cq); 126.1 2C, **Ar**); 126.0 (2C, **Ar**); 114.2 (C, CH); 113.7 (C, CH); 59.3 (C, N–CH_2); 50.1 (C, N–CH); 32.0 ((2C, CH_2–N–CH_2); 21.3 (2C, **2C**H$_3$); 23.6 (2C, CH_2–N–CH_2); 20.5 (1C, CH$_3$); 20.4 (1C, CH$_3$). $C_{23}H_{29}BrN_2$ (M_w = 413.39 g mol^{-1}) HRMS (ESI) ($C_{23}H_{29}N_2^+$) m/z calcd [M + H]$^+$ 333.2331, found 333.23.

*2.1.2.3 3-Cyclopentyl-1-(4-isopropylbenzyl)-5,6-dimethyl-1H-benzo[d]imidazole-3-ium chloride (**A3**).* Yield 80% (610 mg, white solid); m.p. = 178 °C; FT-IR ν(C–N) = 1551 cm^{-1}. ^{1}H NMR (400 MHz, DMSO-d^6, TMS, 298 K): δ (ppm) = 10.26 (s, 1H, NCHN); 7.87 (s, 1H, Ar); 7.78 (s, 1H, Ar); 7.46 (s, H, Ar); 7.26 (s, H, Ar); 5.76 (s, 1H, CH$_3$–CH–CH$_3$); 5.68 (s, 2H, N–CH_2); 5.08 (s, 1H, N–CH–(CH$_2$)); 2.35 (s, 6H, 2CH_3(benzimidazole)); 2.29 (m, 2H, N–CH–CH_2); 2.06 (m, 2H, N–CH–CH_2); 1.90 (m, 2H, CH–CH$_2$–CH_2); 1.76 (m, 2H, CH–CH$_2$–CH_2); 1.16 (s, 6H, CH_3–CH–CH_3). ^{13}C NMR (100 MHz, DMSO-d^6, TMS, 298 K): δ (ppm) = 149.2 (NCHN); 139.9 (C, (CH$_3$)$_2$CH–Cq); 136.8 (C, CH$_3$–Cq); 134.2 (C, CH$_3$–Cq); 130.2 (C, Cq); 130.0 (C, Cq); 129.3 (C, Cq); 128.7 (2C, **Ar**); 127.2 (2C, **Ar**); 114.2 (C, CH); 113.7 (C, CH); 59.3 (C, N–CH_2); 55.4 (C, CH$_3$–CH–CH$_3$); 49.8 (C, N–CH); 32.0 (2C, CH_2–N–CH_2); 24.2 (2C, CH$_3$–CH–CH$_3$); 23.7 (2C, CH_2–N–CH_2); 20.4 (1C, CH$_3$); 20.4 (1C, CH$_3$). $C_{24}H_{31}ClN_2$ (M_w = 382.96 g mol^{-1}) HRMS (ESI) ($C_{24}H_{31}N_2^+$) m/z calcd [M + H]$^+$ 347.2487, found 347.2464.

*2.1.2.4 1-(4-(tert-Butyl)benzyl)-3-cyclopentyl-5,6-dimethyl-1H-benzo[d]imidazole-3-ium chloride (**A4**).* Yield 76% (610 mg, white solid); m.p. = 200 °C; FT-IR ν(C–N) = 1550 cm^{-1}. ^{1}H NMR (400 MHz, DMSO-d^6, TMS, 298 K): δ (ppm) = 10.37 (s, 1H, NCHN); 7.88 (s, 1H, Ar); 7.80 (s, 1H, Ar); 7.47 (s, 2H, Ar); 7.40 (s, 2H, Ar); 5.70 (s, 2H, N–CH_2); 5.09 (s, 1H, N–CH–(CH$_2$)); 2.37 (s, 6H, 2CH_3(benzimidazole)); 2.29 (m, 2H, N–CH–CH_2); 2.06 (m, 2H, N–CH–CH_2); 1.90 (m, 2H, CH–CH$_2$–CH_2); 1.76 (m, 2H, CH–CH$_2$–CH_2); 1.23 (s, 9H, 3CH$_3$(*t*-but)). ^{13}C NMR (100 MHz, DMSO-d^6, TMS, 298 K): δ (ppm) = 151.4 (NCHN); 140.42 (C, CH$_3$–Cq); 136.9 (C, CH$_3$–Cq); 136.8 (C, CH$_3$–Cq); 132.0 (C, Cq); 130.2 (C, Cq); 130.0 (C, Cq); 128.3 (2C, **Ar**); 126.1 (2C, **Ar**); 114.2 (C, CH); 113.7 (C, CH); 59.3 (C, N–CH_2); 49.7 (C, N–CH); 34.7 (C–(CH$_3$)$_3$); 31.4 (3C, C–(CH$_3$)$_3$); 32.0 ((2C, CH_2–N–CH_2); 23.7 (2C, CH_2–N–CH_2); 20.4 (1C, CH$_3$); 20.4 (1C, CH$_3$). $C_{25}H_{33}ClN_2$ (M_w = 396.99 g mol^{-1}) HRMS (ESI) ($C_{25}H_{33}N_2^+$) m/z calcd [M + H]$^+$ 361.2644, found 361.2620.

*2.1.2.5 3-Cyclopentyl-1-(3,5-di-tert-butylbenzyl)-5,6-dimethyl-1H-benzo[d]imidazole-3-ium bromide (**A5**).* Yield 85% (854 mg, white solid); m.p. = 234 °C; FT-IR ν(C–N) = 1556 cm^{-1}. ^{1}H NMR (400 MHz, DMSO-d^6, TMS, 298 K): δ (ppm) = 10.12 (s, 1H, NCHN); 7.90 (s, 1H, Ar); 7.87 (s, 1H, Ar); 7.46 (s, 2H, Ar); 7.33 (s, 2H, Ar); 5.65 (s, 2H, N–CH_2); 5.12 (s, 1H, N–CH–(CH$_2$)); 2.39 (s, 6H, 2CH_3(benzimidazole)); 2.32 (m, 2H, N–CH–CH_2); 2.03 (m, 2H, N–CH–CH_2); 1.88 (m, 2H, CH–CH$_2$–CH_2); 1.78 (m, 2H, CH–CH$_2$–CH_2). ^{13}C NMR (100 MHz, DMSO-d^6, TMS, 298 K): δ (ppm) = 151.5 (2Cq, Cq–(*t*-bu)); 139.7 (NCHN); 136.8 (C, CH$_3$–Cq); 135.9 (C, CH$_3$–Cq); 134.0 (C, Cq); 130.1 (C, Cq); 129.9 (C, Cq); 123.3 (2C, **Ar**); 122.3 (1C, **Ar**); 114.1 (C, CH); 114.0 (C, CH); 59.3 (C, N–CH_2); 50.8 (C, N–CH); 35.0 (2C, C (*t*-bu)); 32.1 (2C, CH_2–N–CH_2); 31.5 (6C, 6 CH$_3$ (*t*-bu)); 23.5 (2C, CH_2–N–CH_2); 20.4 (2C, 2CH_3(benzimidazole)). $C_{29}H_{41}BrN_2$ (M_w = 497.55 g mol^{-1}) HRMS (ESI) ($C_{29}H_{41}N_2^+$) m/z calcd [M + H]$^+$ 417.3270, found 417.3200.

*2.1.2.6 3-Cyclopentyl-5,6-dimethyl-1-(3,4,5-trimethoxybenzyl)-1H-benzo[d]imidazole-3-ium chloride (**A6**).* Yield 82% (712 mg, white solid); m.p. = 180 °C; FT-IR ν(C–N) = 1588 cm^{-1}. ^{1}H NMR (400 MHz, DMSO-d^6, TMS, 298 K): δ (ppm) = 10.37 (s, 1H, NCHN); 7.93 (s, 1H, 1H, Ar); 7.87 (s, 1H, 1H, Ar); 7.05 (s, 2H, Ar); 5.75 (s, 1H, N–CH–(CH$_2$)); 5.60 (s, 2H, N–CH_2); 3.77 (s, 6H, OCH$_3$); 3.60 (s, 6H, OCH$_3$); 2.40 (s, 6H, 2CH_3(benzimidazole)); 2.29 (m, 2H, N–CH–CH_2); 2.08 (m, 2H, N–CH–CH_2); 1.90 (m, 2H, CH–CH$_2$–CH_2); 1.76 (m, 2H, CH–CH$_2$–CH_2). ^{13}C NMR (100 MHz, DMSO-d^6, TMS, 298 K): δ (ppm) = 153.5 (2Cq, Cq–(OCH$_3$)); 140.2 (NCHN); 138.0 (C, OCH$_3$–Cq); 136.8 (C, CH$_3$–Cq); 136.7 (C, CH$_3$–Cq); 130.1 (C, Cq); 129.3 (C, Cq); 128.96 (C, Cq); 125.7 (C, **Ar**); 106.29 (2C, **Ar**); 114.1 (C, CH); 113.9 (C, CH); 60.44 (C, O–CH$_3$); 59.3 (C, N–CH_2); 56.6 (2C, O–CH$_3$); 50.4 (C, N–CH); 32.8 (2C, CH_2–N–CH_2); 23.6 (2C, CH_2–N–CH_2); 20.4 (1C, CH$_3$); 20.4 (1C, CH$_3$). $C_{24}H_{31}ClN_2O_3$ (M_w = 430.96 g mol^{-1}) HRMS (ESI) ($C_{24}H_{31}N_2O_3^+$) m/z calcd [M + H]$^+$ 395.2335, found 395.2310.

2.1.3. General procedure for the synthesis of selenium-NHC compounds (B1–B6). The selenium-NHC complexes were synthesized through the direct reaction of benzimidazolium salts with elemental selenium in the presence of a mild base. In a typical procedure, the benzimidazolium salt (1.0 equiv.) was combined with selenium powder (1.0 equiv.) and potassium carbonate (1.5 equiv.) in methanol. The reaction mixture was stirred at 80 °C for 48 hours, promoting *in situ* carbene generation and subsequent formation of the Se-NHC adducts.[23,24] This transformation proceeded smoothly, resulting in the formation of a black solid, indicating the successful coordination of selenium. The crude product was dissolved in dichloromethane (CH_2Cl_2) and subjected to flash column chromatography on silica gel for purification. After the removal of the solvent by evaporation in open air, the purified compound was recrystallized from a chloroform/diethyl ether mixture (1 : 3, v/v) at room temperature, affording the selenium-NHC complex in solid form.

*2.1.3.1 1-Cyclopentyl-5,6-dimethyl-3-(4-methylbenzyl)-1H-benzo[d]imidazole-2(3H)-selenone (**B1**).* Yield 79% (630 mg, yellow solid); m.p. = 196 °C; FT-IR ν(C–N) = 1251 cm^{-1}. ^{1}H NMR (400 MHz, DMSO-d^6, TMS, 298 K): δ (ppm) = 7.32 (s, 1H, Ar); 7.25 (s, 1H, Ar); 7.25 (s, 2H, Ar); 7.12 (s, 2H, Ar); 5.75 (s, 2H, N–CH_2); 5.61 (s, 1H, N–CH–(CH$_2$)); 2.29 (s, 3H, CH$_3$–Ph); 2.23 (s, 6H, 2CH_3(benzimidazole)); 2.11 (m, 2H, N–CH–CH_2); 2.02 (m, 2H, N–CH–CH_2); 1.90 (m, 2H, CH–CH$_2$–CH_2); 1.74 (m, 2H, CH–CH$_2$–CH_2). ^{13}C NMR (100 MHz, DMSO-d^6, TMS, 298): δ (ppm) = 165.4 (C=Se); 138.4 (C, CH$_3$–Cq); 137.2 (C, CH$_3$–Cq); 137.2 (C, CH$_3$–Cq); 133.4 (C, Cq); 132.2 (C, Cq); 131.98 (C, Cq); 129.85 (2C, **Ar**); 127.8 (2C, **Ar**); 111.9 (C, CH); 111.7 (C, CH); 59.7 (C, N–CH_2); 49.3 (C, N–CH); 28.5 (2C, CH_2–N–CH_2); 25.7 (2C, CH_2–N–CH_2); 21.1 (1C, CH$_3$); 20.2 (1C, CH$_3$); 20.1 (1C, CH$_3$). $C_{22}H_{26}N_2Se$ (M_w = 397.41 g mol^{-1}) HRMS (ESI) m/z ($C_{22}H_{26}N_2Se^+$) calcd [M + H]$^+$ 398.1261, found 398.1234.

*2.1.3.2 1-Cyclopentyl-3-(3,5-dimethylbenzyl)-5,6-dimethyl-1H-benzo[d]imidazole-2(3H)-selenone (**B2**).* Yield 85% (704 mg, yellow solid); m.p. = 154 °C; FT-IR ν(C–N) = 1251 cm^{-1}. ^1H NMR (400 MHz, DMSO-d^6, TMS, 298 K): δ (ppm) = 7.33 (s, 1H, Ar); 7.21 (s, 1H, Ar); 6.94 (s, 2H, Ar); 6.87 (s, H, Ar); 5.81 (s, 1H, CH_2–C*H*–CH_2); 5.57 (s, 2H, N–CH_2); 2.29 (s, 3H, CH_3(benzimidazole)); 2.22 (s, 3H, CH_3(benzimidazole)); 2.19 (s, 6H, 2CH_3(benzyl)); 2.19 (m, 2H, N–CH–CH_2); 2.02 (m, 4H, N–CH–CH_2); 1.74 (m, 2H, CH–CH_2–CH_2). ^{13}C NMR (100 MHz, DMSO-d^6, TMS, 298 K): δ (ppm) = 165.7 (*C*=Se); 138.0 (2Cq, CH_3–*C*q); 136.1 (C, CH_3–*C*q); 132.2 (C, *C*q); 131.9 (C, Cq); 129.4 (C, Cq); 129.3 (C, Cq); 125.4 2C, **Ar**); 125.2 (C, **Ar**); 111.9 (C, *C*H); 113.6 (C, *C*H); 59.7 (C, N–*C*H_2); 49.5 (C, N–*C*H); 28.5 ((2C, CH_2–N–CH_2); 25.0 (2C, CH_2–N–CH_2); 21.4 (2C, **2C**H_3); 20.2 (1C, CH_3); 20.1 (1C, CH_3). $C_{23}H_{28}N_2Se$ (M_w = 411.44 g mol^{-1}) HRMS (ESI) *m*/*z* ($C_{23}H_{28}N_2Se^+$) calcd $[M + H]^+$ 412.1418, found 412.1435.

*2.1.3.3 1-Cyclopentyl-3-(4-isopropylbenzyl)-5,6-dimethyl-1H-benzo[d]imidazole-2(3H)-selenone (**B3**).* Yield 79% (672 mg, yellow solid); m.p. = 88 °C; FT-IR ν(C–N) = 1257 cm^{-1}. ^1H NMR (400 MHz, DMSO-d^6, TMS, 298 K): δ (ppm) = 7.38 (s, 1H, Ar); 7.27 (s, 1H, Ar); 7.17 (s, 4H, Ar); 6.02 (s, 1H, CH_3–C*H*–CH_3); 5.65 (s, 2H, N–CH_2); 5.08 (s, 1H, N–C*H*–(CH_2)); 2.32 (s, 3H, CH_3(benzimidazole)); 2.26 (s, 3H, CH_3(benzimidazole)); 2.12 (m, 2H, N–CH–CH_2); 2.03 (m, 4H, N–CH–CH_2); 1.76 (m, 2H, CH–CH_2–CH_2); 1.21 (s, 6H, CH_3–CH–CH_3). ^{13}C NMR (100 MHz, DMSO-d^6, TMS, 298 K): δ (ppm) = 165.7 (*C*=Se); 148.3 (C, $(CH_3)_2$CH–*C*q); 132.9 (C, CH_3–*C*q); 132.0 (C, Cq); 131.6 (C, Cq); 129.5 (C, Cq); 127.4 (2C, **Ar**); 126.7 (2C, **Ar**); 111.6 (C, *C*H); 111.1 (C, *C*H); 59.9 (C, N–*C*H_2); 55.4 (C, CH_3–*C*H–CH_3); 50.1 (C, N–*C*H); 28.6 (2C, CH_2–N–CH_2); 25.3 (2C, *C*H_3–CH–*C*H_3); 23.9 (2C, CH_2–N–CH_2); 20.4 (1C, CH_3); 20.1 (1C, CH_3). $C_{24}H_{30}N_2Se$ (M_w = 425.46 g mol^{-1}) HRMS (ESI) ($C_{24}H_{30}N_2Se^+$) *m*/*z* calcd $[M + H]^+$ 426.1574, found 426.1562.

*2.1.3.4 1-(4-(tert-Butyl)benzyl)-3-cyclopentyl-5,6-dimethyl-1H-benzo[d]imidazole-2(3H)-selenone (**B4**).* Yield 89% (784 mg, brown solid); m.p. = 165–166 °C; FT-IR ν(C–N) = 1263 cm^{-1}. ^1H NMR (400 MHz, DMSO-d^6, TMS, 298 K): δ (ppm) = 7.32 (s, 6H, Ar); 5.82 (s, 1H, N–C*H*–(CH_2)); 5.61 (s, 2H, N–CH_2); 2.30 (s, 3H, CH_3(benzimidazole)); 2.24 (s, 3H, CH_3(benzimidazole)); 2.11 (m, 2H, N–CH–CH_2); 2.02 (m, 2H, N–CH–CH_2); 1.90 (m, 2H, CH–CH_2–CH_2); 1.74 (m, 2H, CH–CH_2–CH_2); 1.22 (s, 9H, 3CH_3(*t*-but)). ^{13}C NMR (100 MHz, DMSO-d^6, TMS, 298 K): δ (ppm) = 165.5 (*C*=Se); 150.4 (C, CH_3–*C*q); 133.6 (C, CH_3–*C*q); 132.6 (C, Cq); 131.9 (C, Cq); 129.3 (C, Cq); 127.6 (2C, **Ar**); 125.7 (2C, **Ar**); 111.9 (C, *C*H); 111.7 (C, *C*H); 55.3 (C, N–*C*H_2); 55.4 (C, N–*C*H); 49.1 (C, N–*C*H); 34.6 (*C*–$(CH_3)_3$); 31.5 (3C, C–(*C*H_3)$_3$); 28.5 (2C, CH_2–N–CH_2); 25.0 (2C, CH_2–N–CH_2); 20.2 (1C, *C*H_3); 20.1 (1C, *C*H_3). $C_{25}H_{32}N_2Se$ (M_w = 439.49 g mol^{-1}) HRMS (ESI) ($C_{25}H_{32}N_2Se^+$) *m*/*z* calcd $[M + H]^+$ 440.1731, found 440.1697.

*2.1.3.5 1-Cyclopentyl-3-(3,5-di-tert-butylbenzyl)-5,6-dimethyl-1H-benzo[d]imidazole-2(3H)-selenone (**B5**).* Yield 83% (824 mg, yellow solid); m.p. = 166 °C; FT-IR ν(C–N) = 1245 cm^{-1}. ^1H NMR (400 MHz, DMSO-d^6, TMS, 298 K): δ (ppm) = 7.42 (s, 2H, Ar); 7.35 (s, 1H, Ar); 7.31 (s, 1H, Ar); 7.25 (s, 1H, Ar); 5.75 (s, 1H, N–C*H*–(CH_2)); 5.62 (s, 2H, N–CH_2); 2.29 (s, 6H, 2CH_3(benzimidazole)); 2.10 (m, 2H, N–CH–CH_2); 2.02 (m, 2H, N–CH–CH_2); 1.97 (m, 2H, CH–CH_2–CH_2); 1.74 (m, 2H, CH–CH_2–CH_2); 1.21 (s, 18H, 6CH_3(*t*-but)). ^{13}C NMR (100 MHz, DMSO-d^6, TMS, 298 K): δ (ppm) = 165.4 (*C*=Se); 150.8 (2Cq, Cq–(*t*-bu)); 135.3 (C, CH_3–*C*q); 132.1 (C, Cq); 131.8 (C, Cq); 129.3 (C, Cq); 122.9 (2C, **Ar**); 121.4 (1C, **Ar**); 111.9 (C, *C*H); 111.8 (C, *C*H); 59.7 (C, N–*C*H_2); 49.9 (C, N–*C*H); 34.9 (2C, C (*t*-bu)); 31.6 (6C, 6 *C*H_3 (*t*-bu)); 28.4 (2C, CH_2–N–CH_2); 24.9 (2C, CH_2–N–CH_2); 20.4 (2C, CH_3(-benzimidazole); 20.1 (2C, CH_3(benzimidazole)). $C_{29}H_{40}N_2Se$ (M_w = 495.60 g mol^{-1}) HRMS (ESI) ($C_{29}H_{40}N_2Se^+$) *m*/*z* calcd $[M + H]^+$ 496.2357, found 496.2349.

*2.1.3.6 1-Cyclopentyl-5,6-dimethyl-3-(3,4,5-trimethoxybenzyl)-1H-benzo[d]imidazole-2(3H)-selenone (**B6**).* Yield 72% (688 mg, yellow solid); m.p. = 166 °C; FT-IR ν(C–N) = 1224 cm^{-1}. ^1H NMR (400 MHz, DMSO-d^6, TMS, 298 K): δ (ppm) = 7.41 (s, 1H, Ar); 7.32 (s, 1H, Ar); 6.89 (s, 2H, Ar); 5.74 (s, 1H, N–C*H*–(CH_2)); 5.57 (s, 2H, N–CH_2); 3.69 (s, 6H, OCH_3); 3.60 (s, 3H, OCH_3); 2.29 (s, 3H, CH_3(benzimidazole)); 2.26 (s, 3H, CH_3(benzimidazole)); 2.12 (m, 2H, N–CH–CH_2); 2.01 (m, 4H, N–CH–CH_2–CH_2); 1.73 (m, 2H, CH–CH_2–CH_2). ^{13}C NMR (100 MHz, DMSO-d^6, TMS, 298 K): δ (ppm) = 165.4 (*C*=Se); 153.2 (2Cq, Cq–(OCH_3)); 137.4 (C, OCH_3–*C*q); 132.3 (C, CH_3–*C*q); 132.3 (C, CH_3–*C*q); 132.2 (C, Cq); 131.8 (C, Cq); 129.3 (C, Cq); 111.9 (C, *C*H); 111.8 (C, *C*H); 105.6 (2C, **Ar**); 60.4 (C, O–*C*H_3); 59.8 (C, N–*C*H_2); 56.3 (2C, O–*C*H_3); 49.5 (C, N–*C*H); 28.4 (2C, CH_2–N–CH_2); 25.0 (2C, CH_2–N–CH_2); 20.1 (1C, CH_3); 20.1 (1C, CH_3). $C_{24}H_{30}N_2O_3Se$ (M_w = 473.46 g mol^{-1}) HRMS (ESI) ($C_{24}H_{30}N_2O_3Se^+$) *m*/*z* calcd $[M + H]^+$ 474.1422, found 474.1431.

2.2. Biological assays

2.2.1. Materials. The anticancer activity experiments were conducted in the Laboratory of the Department of Molecular Biology and Genetics, Inonu University, Malatya, Türkiye. The study utilized various chemical materials, including MTT (3-(4,5-dimethylthiazol-2-yl)-2,5-diphenyltetrazolium bromide) for cell viability assays, phosphate-buffered saline (PBS, pH 7.4) for washing cell monolayers, and trypsin-EDTA solution for detaching adherent cells. Dulbecco's Modified Eagle Medium (DMEM), supplemented with 10% fetal bovine serum (FBS) and 1% penicillin–streptomycin, was used for routine cell culture. Dimethyl sulfoxide (DMSO) and dimethylformamide (DMF) were used as solvents for compound preparation when necessary. The human cell lines used in this study included HCT116 (ATCC CCL-247, human colon carcinoma), SH-SY5Y (ATCC CRL-2266, human neuroblastoma), and BEAS-2B (ATCC CRL-3588, human bronchial epithelial, non-cancerous). All cell lines were commercially obtained from American Type Culture Collection ATCC and maintained in the Medical Genetics Laboratory, Faculty of Medicine, Inonu University. Experiments were performed using 96-well plates in a humidified incubator (MCO-170AC-PE) maintained at 37 °C with 5% CO_2. A hemocytometer was used for cell counting, and absorbance measurements were performed with an ELISA microplate reader (BioTek Epoch) set at 570 and 630 nm.

2.2.2. Anticancer (MTT) test. The anticancer properties of the samples were evaluated using the MTT assay, following the procedure described by Sharma *et al.*[25] The cytotoxic activity was

tested against three cell lines: HCT116, SH-SY5Y, and BEAS-2B. Cells were cultured in Dulbecco's Modified Eagle Medium (DMEM) supplemented with 10% fetal bovine serum (FBS) and 1% penicillin–streptomycin, and maintained at 37 °C in a humidified atmosphere containing 5% CO_2. Once the cells reached 70–80% confluency, the culture medium was removed, and the monolayer was washed several times with sterile phosphate-buffered saline (PBS, pH 7.4). Trypsin-EDTA was added to detach the cells, and after 5 minutes of incubation at 37 °C, enzymatic activity was neutralized by adding twice the volume of fresh medium. The resulting suspension was centrifuged at 1000 rpm for 7 minutes, and the cell pellet was resuspended in 5 mL of fresh medium. Cells were counted and adjusted to a final concentration of 1×10^5 cells per mL, and 100 μL of the suspension (1×10^4 cells) was seeded into each well of a 96-well plate. After 24 hours of incubation at 37 °C in 5% CO_2 to allow cell adhesion, the compounds were tested for anticancer activity. The test samples were prepared by diluting the stock solutions in fresh medium to obtain a concentration range of 0.8–800 μg mL^{-1}. Following removal of the old medium, 100 μL of the compound-containing medium was added to each well, and plates were incubated for 24 hours under the same conditions. Subsequently, the treatment medium was removed, and 10 μL of MTT solution (5 mg mL^{-1}) along with 90 μL of fresh medium were added to each well, resulting in a final MTT concentration of 0.5 mg mL^{-1}. After 4 hours of incubation at 37 °C, absorbance was measured at 570 nm and 630 nm using a microplate (ELISA) reader. Cell viability (%) was calculated using the formula:

$$[(Abs_{570} - Abs_{630}) \text{ of treated cells}/(Abs_{570} - Abs_{630}) \text{ of control cells}] \times 100.$$

IC_{50} values were determined from dose–response curves based on logarithmic transformation of the viability data.

2.3. Computational details

2.3.1. Quantum chemical calculations. All quantum chemical calculations were performed using Density Functional Theory (DFT) as implemented in the Gaussian 09 software package.[26] The geometries of all investigated molecules were fully optimized at the B3LYP/6-311G(d,p) level of theory without imposing any symmetry constraints. Vibrational frequency calculations were carried out at the same level to confirm that the optimized structures correspond to true minima on the potential energy surface (no imaginary frequencies). All DFT calculations were performed in water using the SMD (Solvation Model based on Density) continuum solvation model as implemented in Gaussian 09 to include solvent polarization effects. The frontier molecular orbital (FMO) energies (ε_{HOMO} and ε_{LUMO}) obtained from the optimized geometries were used to evaluate several global reactivity descriptors, including:

$$I = -\varepsilon_{HOMO} \text{ (ionization energy)}$$

$$A = -\varepsilon_{LUMO} \text{ (electron affinity)}$$

$$\eta = (I - A)/2 \text{ (chemical hardness)}$$

$$\mu = -(I + A)/2 \text{ (chemical potential)}$$

$$\chi = (I + A)/2 \text{ (electronegativity)}$$

$$\sigma = 1/\eta \text{ (chemical softness)}$$

$$\omega = \mu^2/(2\eta) \text{ (electrophilicity index)}$$

$$\xi = 1/\omega \text{ (nucleophilicity index)}$$

The Fukui functions and related local reactivity parameters were calculated using the Multiwfn 3.8 program,[27] based on the finite difference approach. The visualization of molecular orbitals, electron density, and Fukui function maps was performed using VMD 1.9.3.[28]

2.3.2. Docking procedure. The molecular docking simulations were conducted to investigate the binding affinity and interaction modes of the studied ligands with selected target proteins. Ligand preparation was performed using AutoDockTools (ADT).[29] All ligand structures were converted to the PDBQT format after the addition of Gasteiger charges and definition of rotatable bonds (torsional degrees of freedom).

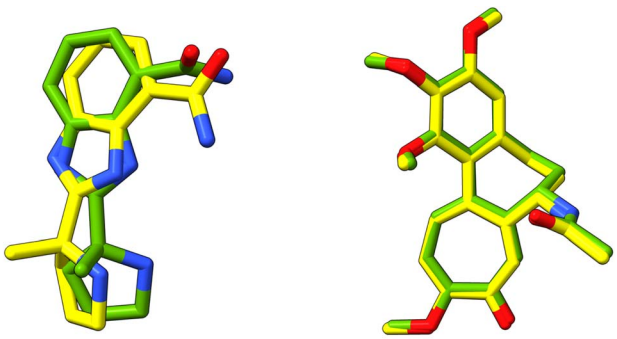

Receptor	PDB ID	Center X	Center Y	Center Z
PARP-1	5LX6	42.55	49.49	82.93
Tubulin	4O2B	17.01	65.99	43.39

Fig. 1 Validation of the molecular docking protocol. (a) Superposition of the crystallographic (green) and docked (yellow) conformations of the native ligand veliparib within the active site of PARP-1 (PDB ID: 5LX6). (b) Superposition of the crystallographic (green) and docked (yellow) conformations of colchicine bound to tubulin (PDB ID: 4O2B). The RMSD values and grid box parameters used for each receptor are summarized in the inset table.

The protein structures were retrieved from the RCSB Protein Data Bank (RCSB PDB) using their corresponding PDB IDs. Prior to docking, all crystallographic water molecules were removed, polar hydrogens were added, and Gasteiger charges were assigned. The processed receptor structures were then converted into the PDBQT format for docking calculations. Docking simulations were performed using AutoDock Vina 1.2.7.[30] The grid box parameters were defined manually to cover the active sites of the target proteins, as summarized in Fig. 1. Each docking calculation was carried out with an exhaustiveness value of 32, ensuring thorough sampling of the conformational space. The best-ranked binding pose for each ligand was selected based on the Vina scoring function (binding affinity in kcal mol^{-1}). The resulting complexes were analyzed to examine ligand–receptor interactions and binding modes. The root mean square deviation (RMSD) between the docked pose of the native ligand and its crystallographic conformation was also calculated to validate the accuracy and reliability of the docking protocol (Fig. 1).

3. Results and discussion

3.1. Synthesis

The synthesis of NHC-type ligands and their metal complexes, including selenium derivatives, has been previously reported in

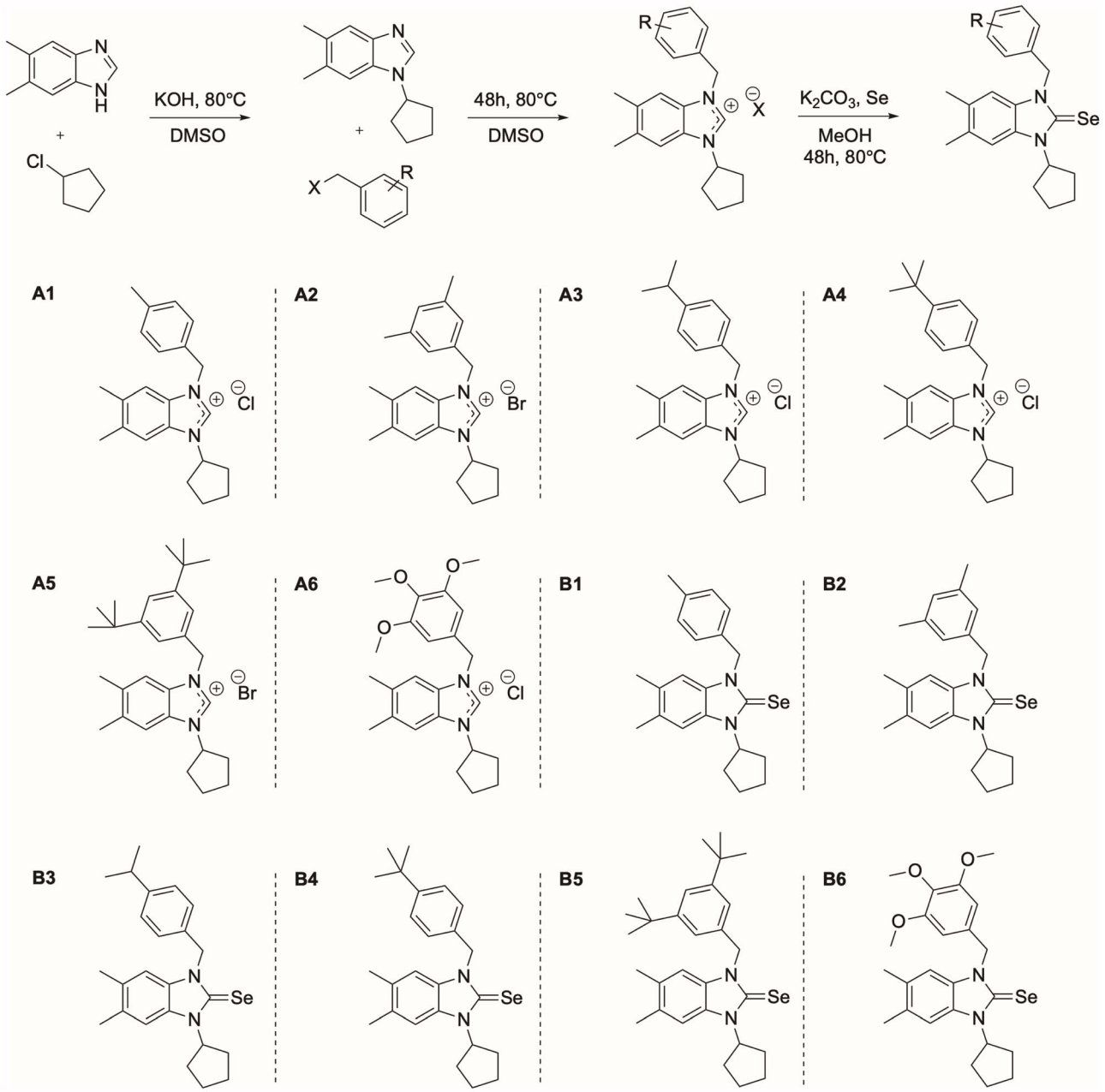

Scheme 1 Synthetic pathway for the preparation of benzimidazolium-based NHC ligands (A1–A6) and their corresponding selenium-NHC complexes (B1–B6) starting from benzimidazole as the precursor.

the literature.[31,32] In the present work, similar synthetic procedures were adopted with certain modifications to optimize reaction efficiency and product yield. The overall synthetic route involved four main steps, starting from a benzimidazole derivative as the initial precursor and leading to the final selenium-NHC complexes, as outlined in Scheme 1.

The benzimidazolium salts (**A1–A6**) were synthesized through a two-step *N*-alkylation process starting from commercially available 1*H*-benzimidazole derivative (Scheme 1). In the first step, *N*-alkylation with 1-chloromethylcyclopentane in the presence of potassium hydroxide (KOH) afforded the mono-alkylated intermediate 1-cyclopentyl-1*H*-benzo[*d*]imidazole. This intermediate was subsequently subjected to a second alkylation with various aryl or benzyl halides in DMF at 80 °C, leading to the formation of the benzimidazolium salts **A1–A6** after purification. The method proved efficient and reproducible, yielding structurally diverse NHC precursors (76–85%) suitable for further functionalization and biological evaluation.

All salts (**A1–A6**) were isolated as white crystalline solids with melting points ranging from 174 °C to 234 °C, consistent with their ionic nature and the stability of the benzimidazolium framework. Compound **A5** exhibited the highest melting point (234 °C) and yield (85%), likely due to enhanced intermolecular interactions from its bulky *tert*-butyl substituents. The spectroscopic data were in good agreement with literature values for related compounds,[33] confirming successful quaternization. All salts were stable under air and moisture, showing no decomposition even after prolonged storage.

The structures of the benzimidazolium salts were confirmed by spectroscopic analyses. In the ^{1}H NMR spectra, all compounds exhibited a characteristic singlet between δ 10.0–10.4 ppm corresponding to the imidazolium C2–H proton, a characteristic signal confirming successful formation of the cationic species. Aromatic protons appeared as multiplets at δ 6.9–7.9 ppm, while aliphatic *N*-alkyl protons resonated between δ 0.8–4.5 ppm. In the ^{13}C NMR spectra, the imidazolium C2 carbon appeared at δ 139–151 ppm, with aromatic carbons between δ 113–140 ppm and aliphatic carbons at δ 20–60 ppm. These results are consistent with reported data for benzimidazolium analogues. FT-IR spectra of **A1–A6** showed strong bands at 3120–3160 cm^{-1} (aromatic C–H stretching), 1550–1620 cm^{-1} (C=N and C=C stretching of the benzimidazole ring), and 2850–2950 cm^{-1} (aliphatic C–H stretching), confirming alkylation at the nitrogen center. HRMS (ESI$^+$) spectra displayed intense $[M + H]^+$ peaks matching the calculated molecular weights with deviations below ±0.03 (*e.g.*, **A1**: calcd = 319.2174, found = 319.2150), confirming the expected molecular compositions and high purity.

The corresponding selenium-NHC complexes (**B1–B6**) were obtained by reacting the benzimidazolium salts (**A1–A6**) with elemental selenium in the presence of potassium carbonate (K_2CO_3) in methanol at 80 °C (Scheme 1). The base-mediated *in situ* deprotonation at the C2 position generated the free carbene, which subsequently coordinated with selenium to yield the Se-NHC adducts. The reactions proceeded smoothly over 48 h, affording yellow to brown solids in excellent yields (72–89%). The color change from white (salts) to yellow/brown (complexes) provided a clear visual indication of successful complexation. The obtained compounds were stable, easily handled, and soluble in halogenated solvents, facilitating purification.

Upon selenium coordination, the ^{1}H NMR spectra of the complexes (**B1–B6**) showed complete disappearance of the imidazolium C2–H signal ($\delta \approx 10$ ppm), confirming deprotonation and carbene formation. In the ^{13}C NMR spectra, a new resonance appeared at δ 165–166 ppm, characteristic of the carbene carbon bonded to selenium (C–Se), replacing the imidazolium C2 signal of the precursors. Aromatic and aliphatic resonances were consistent with those observed in the ligands, indicating structural integrity of the benzimidazole framework. The FT-IR spectra of **B1–B6** revealed a marked shift of the C–N stretching band from 1550–1588 cm^{-1} in **A1–A6** to 1224–1263 cm^{-1} after coordination, reflecting electron density redistribution around the imidazole ring and confirming C–Se bond formation. These findings are in excellent agreement with reported Se-NHC systems.[34–36] HRMS (ESI$^+$) analyses of **B1–B6** displayed $[M + H]^+$ molecular ion peaks consistent with calculated masses (*e.g.*, **B1**: calcd = 398.1261, found = 398.1234), validating the proposed structures and confirming the successful incorporation of selenium. The absence of signals attributable to protonated imidazolium cations confirmed complete deprotonation and the formation of neutral Se-NHC species.

3.2. Cytotoxicity evaluation

The cytotoxicity of the synthesized benzimidazolium ligands (**A1–A6**) and their corresponding selenium complexes (**B1–B6**) was assessed against two human cancer cell lines—colon cancer (HCT116) and neuroblastoma (SH-SY5Y)—as well as on a non-cancerous lung epithelial cell line (BEAS-2B), using the MTT assay. Cytotoxic effects were quantified by determining the IC_{50} values and compared with those of cisplatin, a clinically used chemotherapeutic agent. The results are presented in Fig. 2, and the detailed IC_{50} values are summarized in Table S1.

The benzimidazolium salts, particularly **A1–A5**, demonstrated significantly higher cytotoxicity toward the tested cancer cell lines compared to cisplatin. Although these compounds also showed considerable toxicity toward the non-cancerous BEAS-2B cells (IC_{50} = 10.71–54.11 μM), the effects of some of them were notably stronger on the cancer cells. For example, **A3** was approximately five times more toxic to SH-SY5Y neuroblastoma cells and twice as toxic to HCT116 colon cancer cells as it was to BEAS-2B cells. This observed selectivity suggests a preferential action against malignant cells, underscoring the promising anticancer potential of the synthesized benzimidazolium salts. Further optimization of their chemical structure could help enhance this selectivity and reduce unwanted toxicity toward normal cells. Among the tested ligands, **A6** exhibited a cytotoxic profile most similar to that of cisplatin, with IC_{50} values of 221.47 ± 15.76 μM for SH-SY5Y and 297.13 ± 15.38 μM for HCT116, close to those of cisplatin (152.12 ± 4.65 μM and 310.12 ± 3.09 μM, respectively). Notably, **A6** displayed

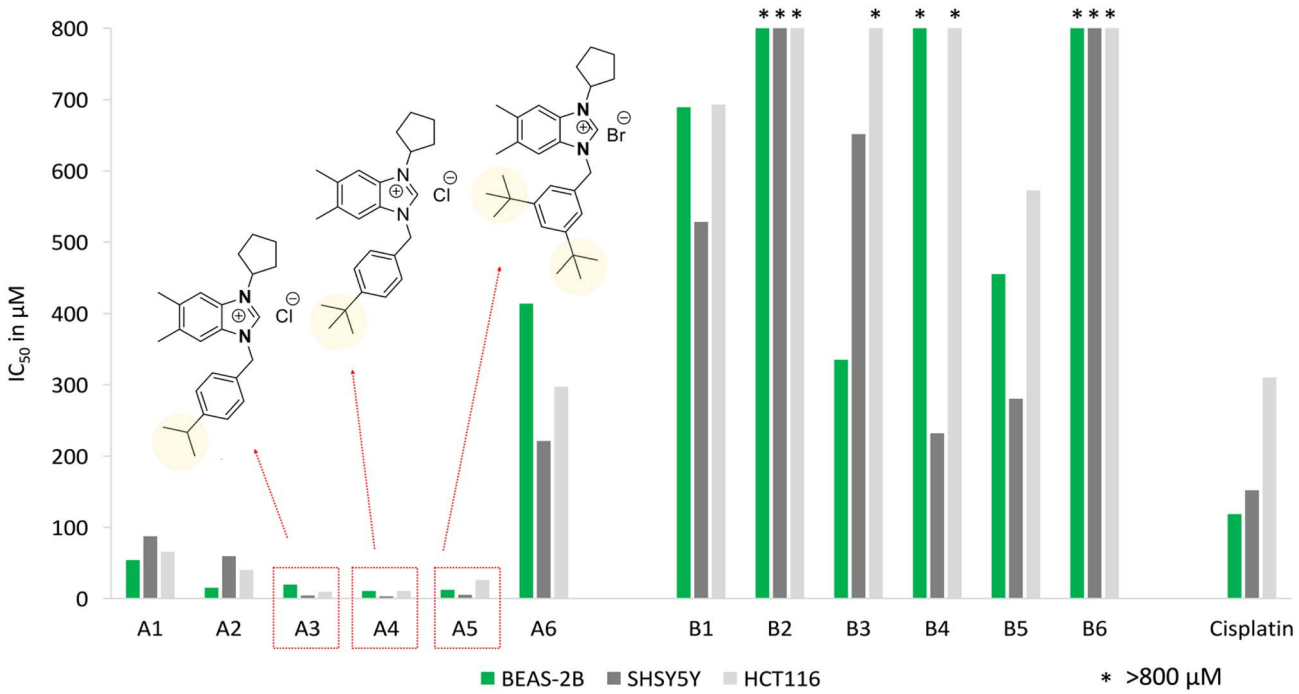

Fig. 2 Cytotoxic activity of benzimidazolium ligands (**A1–A6**) and their selenium complexes (**B1–B6**) against HCT116, SH-SY5Y, and BEAS-2B cell lines determined by the MTT assay. Data are expressed as IC_{50} values and compared with cisplatin as a reference drug.

a much lower toxicity toward BEAS-2B cells (IC_{50} = 413.91 ± 15.63 µM), suggesting that it may represent a potential anticancer candidate with a more favorable safety profile. In contrast, the selenium-NHC complexes (**B1–B6**) showed markedly lower cytotoxicity against all tested cell lines, with IC_{50} values generally above 200 µM, and several compounds exhibiting no detectable activity at the tested concentrations. While these results are less encouraging in terms of anticancer activity, they are nonetheless meaningful. The low toxicity of these selenium derivatives could make them valuable as biocompatible scaffolds or as leads for the development of non-toxic therapeutic agents in future studies.

The comparison between the benzimidazolium salts and their selenium complexes reveals a clear influence of complexation on cytotoxic behavior. The coordination of selenium to the benzimidazolium ligands, which effectively neutralizes their cationic nature, led to a marked decrease in cytotoxicity across all tested cell lines. This observation suggests that the ionic (cationic) character of the benzimidazolium salts plays an important role in their cytotoxic effects, possibly facilitating stronger interactions with negatively charged cellular membranes or biomolecules. A second key factor influencing activity is the nature and number of substituents on the aromatic ring. An increase in the number and bulkiness of alkyl substituents appeared to enhance cytotoxicity. For example, compound **A1**, bearing a single *para*-methyl group, exhibited lower cytotoxicity than compound **A5**, which contains two *tert*-butyl substituents. This trend indicates that an increase in the lipophilic character of the aromatic substituents promotes cellular uptake or membrane affinity, thereby enhancing cytotoxic potency. These findings highlight that both the cationic nature of the benzimidazolium core and the lipophilic character of the aromatic substituents are crucial structural features governing the cytotoxic activity of these compounds.

3.3. *In silico* investigations

In silico investigations were performed for compounds **A1–A6**, which exhibited the most promising cytotoxic activity. Both DFT and molecular docking simulations were employed. The DFT calculations were carried out to determine the optimized molecular geometries of the compounds and to estimate their chemical reactivity and potential interaction behavior toward biological targets. The docking simulations were conducted to gain insights into the ability of these compounds to act as potential inhibitors of two biological targets known to be associated with the anticancer activity of related molecules.

3.3.1. Molecular geometry and chemical reactivity. The molecular geometries of compounds **A1–A6** were optimized using DFT calculations at the B3LYP/6-311G(d,p) level of theory. The optimized structures are presented in Fig. 3. All calculations were performed using water as the solvent environment; therefore, the counterions (Cl^- or Br^-) were not explicitly included, as they are expected to remain solvated and dissociated under physiological conditions and should not markedly affect the intrinsic reactivity of the cation. However, we note that in specific cases, ion-pair interactions may influence the behavior of the compounds, and this potential effect cannot be completely excluded.

Using the optimized geometries, the frontier molecular orbitals (FMOs) of compounds **A1–A6** were computed to gain

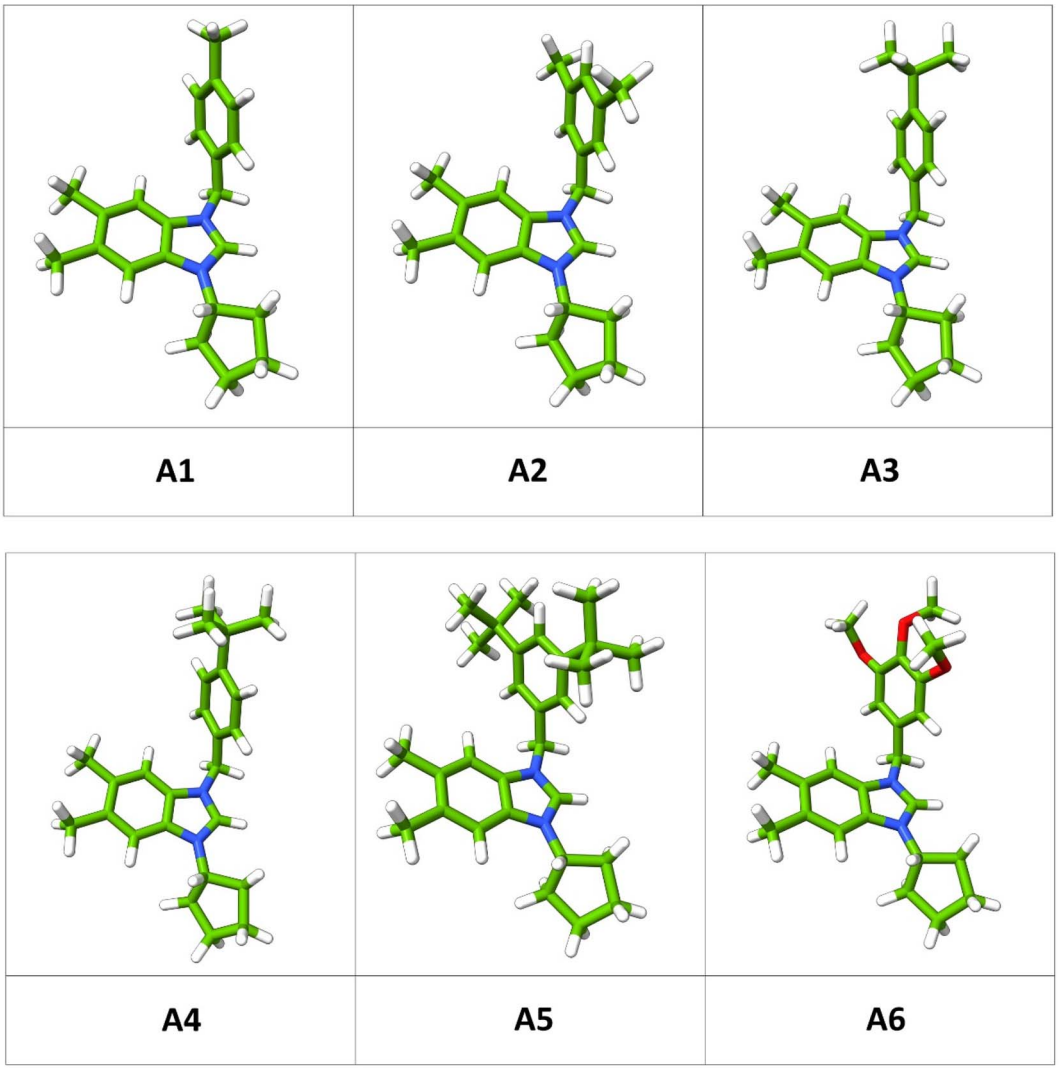

Fig. 3 Optimized molecular geometries of compounds **A1–A6** obtained at the B3LYP/6-311G(d,p) level of theory in aqueous phase using the SMD solvation model. All structures are shown in their optimized cationic forms.

insight into their electronic distribution and potential reactive sites. The HOMO (Highest Occupied Molecular Orbital) and LUMO (Lowest Unoccupied Molecular Orbital) energies are key parameters that describe a molecule's chemical reactivity and stability. The HOMO represents the ability of a molecule to donate electrons, while the LUMO indicates its capacity to accept electrons. Therefore, a smaller HOMO–LUMO energy gap generally corresponds to higher chemical reactivity and lower kinetic stability.[37] The energy levels and spatial distributions of these orbitals are illustrated in Fig. 4. From the obtained results, all compounds exhibit a similar electronic pattern. The HOMO is mainly localized on the substituted benzene ring attached at the N3 position, whereas the LUMO is predominantly distributed over the benzimidazolium moiety, especially around the carbene carbon atom. This distribution suggests that the benzimidazole unit constitutes the most favorable site for nucleophilic attack, while the aromatic substituent is more susceptible to electrophilic attack.

The Fukui functions, depicted in Fig. 4, provide complementary information regarding local reactivity. Derived from conceptual DFT, Fukui functions describe how the electron density of a molecule changes upon addition or removal of an electron, thereby identifying the most reactive atomic sites toward electrophilic or nucleophilic attack. Specifically, the f^- function highlights regions prone to nucleophilic attack, while the f^+ function marks regions favorable for electrophilic attack. The f^- values of **A6**, as representative molecule, are mainly localized on the aromatic ring, confirming its nucleophilic character, whereas the f^+ values are concentrated on the benzimidazole ring, particularly on the carbene carbon, identifying it as the most electrophilic center. The dual descriptor (Δf) further supports these observations, with positive regions (electrophilic) located on the benzimidazole moiety and negative regions (nucleophilic) on the substituted benzene ring. The cycloalkanone fragment shows limited involvement in the

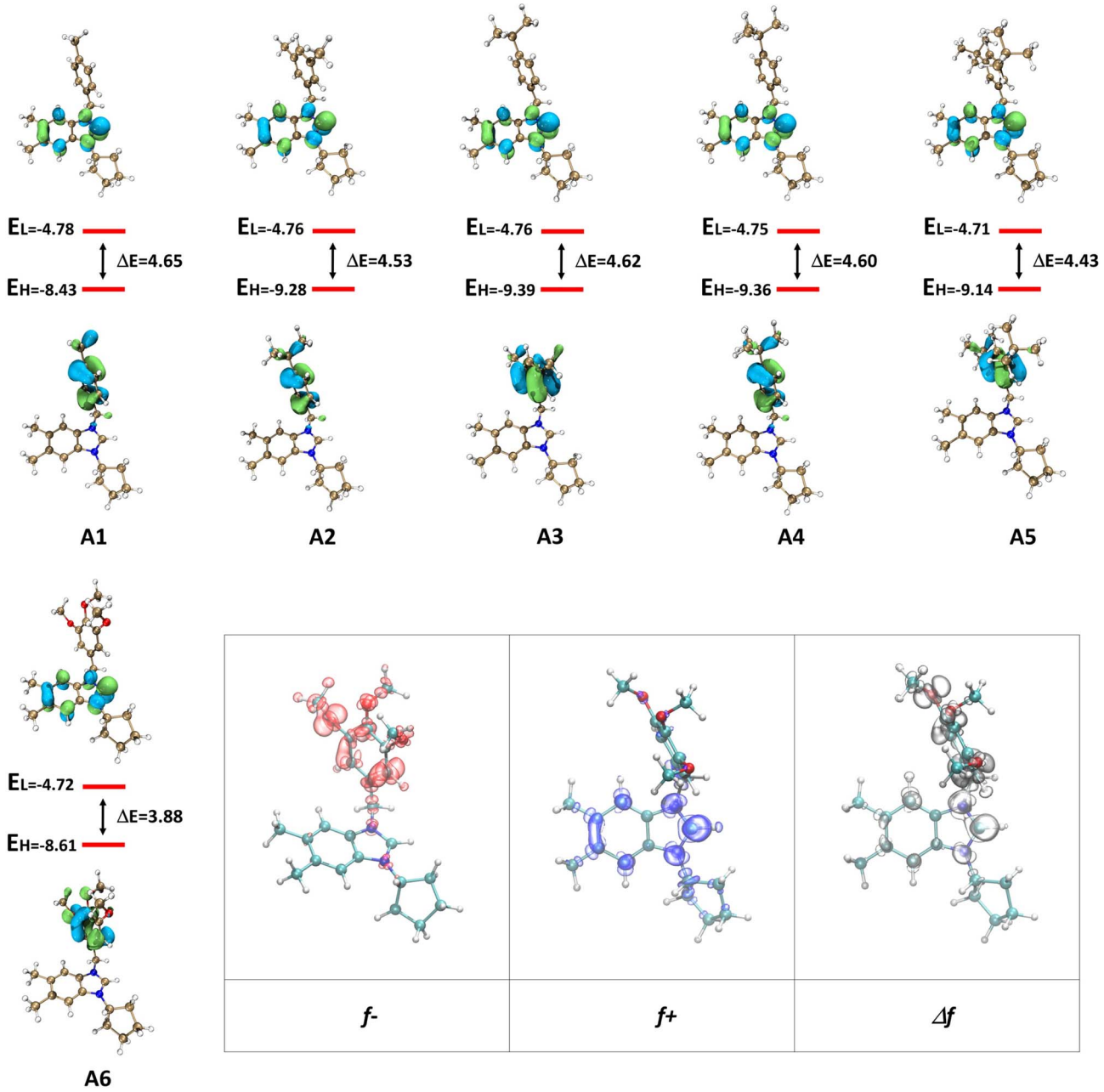

Fig. 4 Distribution and energies of the HOMO and LUMO orbitals for compounds **A1–A6**, together with the Fukui function maps (f^-, f^+, and Δf) for compound **A6**, obtained from DFT calculations at the B3LYP/6-311G(d,p)/SMD(water) level.

frontier orbital density, indicating minimal contribution to the overall reactivity.

The computed HOMO, LUMO, and HOMO–LUMO energy gap (ΔE) values for compounds **A1–A6** are reported in Fig. 4. The HOMO energies range from −9.43 eV (**A1**) to −8.61 eV (**A6**), while the LUMO energies lie between −4.78 eV and −4.71 eV. The resulting energy gaps (ΔE) span 3.88–4.65 eV, indicating moderate molecular stability and a balanced reactivity profile across the series. The consistently low HOMO energies observed for all compounds indicate that these benzimidazolium derivatives are poor electron donors, which is typical for cationic species. Their positive charge delocalization reduces the electron density in the frontier orbitals, making them less prone to losing electrons. Conversely, the low LUMO energy values suggest that these molecules are highly susceptible to accepting electrons, reflecting a strong electrophilic character. Such dual behavior—low electron-donating and strong electron-accepting ability—is characteristic of π-conjugated cationic systems, which can efficiently interact with nucleophilic sites in biological macromolecules.

Among the studied compounds, **A1** exhibits the largest energy gap (4.65 eV), implying the highest kinetic stability and lowest chemical reactivity. In contrast, **A6** displays the smallest gap (3.88 eV), suggesting that it is the most chemically reactive

and electronically polarizable compound of the series. The gradual narrowing of the HOMO–LUMO gap from **A1** to **A6** indicates an increasing ability to participate in charge-transfer interactions, which may enhance biological affinity and reactivity toward enzyme active sites. Overall, the FMO results demonstrate that these benzimidazolium cations are electrophilic in nature, with the benzimidazole ring acting as the principal electron-accepting region. The observed electronic characteristics are in excellent agreement with the Fukui function analysis, which similarly highlights the benzimidazole core as the most reactive site toward nucleophilic attack.

The global reactivity descriptors derived from the frontier molecular orbitals which provide valuable insights into the electronic behavior and chemical reactivity of the benzimidazolium compounds have been computed and they are summarized in Table 1. The ionization potential (I) represents the energy required to remove an electron from a molecule and reflects its electron-donating ability. The relatively high I values (8.61–9.43 eV) indicate that these cationic compounds are poor electron donors, which is consistent with their positive charge and overall electron deficiency. Conversely, the electron affinity (A) values (4.71–4.78 eV) are also relatively high, suggesting that the compounds are energetically favorable electron acceptors, capable of interacting efficiently with nucleophilic or electron-rich sites of biological targets. The chemical hardness (η) and softness ($\sigma = 1/\eta$) describe the resistance or ease of deformation of the electron cloud during chemical reactions. The moderate η values (1.94–2.33 eV) and corresponding σ values (0.43–0.51 eV^{-1}) indicate that these compounds exhibit a balanced reactivity—neither too inert nor too reactive—allowing them to undergo stable yet favorable electronic interactions. The chemical potential (μ), which represents the escaping tendency of electrons, is negative for all compounds (−6.67 to −7.10 eV), confirming the overall electronic stability and the spontaneous flow of electrons from the molecule toward electrophilic centers. The electronegativity (χ) values (6.67–7.10 eV) are consistent with the observed electron-withdrawing nature of the benzimidazolium core, while the electrophilicity index (ω), ranging from 10.81 to 11.44 eV, reveals that all the studied compounds possess a marked electrophilic character. Notably, compound **A6** exhibits the lowest hardness and highest electrophilicity, implying that it is the most chemically reactive. The electrofugality (ξ) values are similar across the series (≈ 0.09), confirming comparable tendencies for electron loss among the compounds. Overall, the descriptors collectively show that the benzimidazolium derivatives are electron-deficient, electrophilic species with a moderate capacity for electronic polarization, supporting their potential for interactions with nucleophilic residues at biological receptor sites.

3.3.2. Docking studies. Two principal molecular targets were selected to explore the potential anticancer mechanism of the synthesized benzimidazolium compounds **A1–A6**, namely tubulin and poly(ADP-ribose) polymerase-1 (PARP-1). Benzimidazole derivatives are well-known tubulin polymerization inhibitors that bind to the colchicine site, disrupting microtubule dynamics and inducing G_2/M cell-cycle arrest, a hallmark of mitotic inhibition.[38–40] In parallel, several benzimidazole-based compounds, including the clinical candidate veliparib (ABT-888), have been reported as potent PARP-1 inhibitors, impairing DNA damage repair and enhancing cancer-cell sensitivity to genotoxic stress.[41,42] These two well-validated targets thus represent complementary mechanisms—tubulin disruption and DNA-repair inhibition—through which benzimidazole derivatives, and potentially the present benzimidazolium derivatives, may exert their antiproliferative activity. The binding energies of compounds **A1–A6**, compared with those of the native ligands, toward the two selected targets are presented in Table 2, while the predicted binding modes within the active sites of the enzymes are illustrated in Fig. 5 and 6.

The data of Table 2 reveal that all the investigated benzimidazolium derivatives exhibit favorable binding affinities toward both PARP-1 and tubulin, with binding energies ranging from −8.96 to −11.25 kcal mol^{-1}, which are comparable to or better than those of the reference ligands. For the PARP-1 target, compound **A5** shows the strongest interaction (−11.25 kcal mol^{-1}), surpassing that of the native inhibitor Veliparib (−8.40 kcal mol^{-1}), suggesting a high potential for

Table 2 Predicted binding energies (kcal mol^{-1}) of benzimidazolium compounds A1–A6 compared with the native ligands veliparib and colchicine against PARP-1 (PDB ID: 5LX6) and tubulin (PDB ID: 4O2B) obtained from AutoDock Vina simulations

Compound	PARP-1 (5LX6)	Tubulin (4O2B)
A1	−9.93	−9.24
A2	−9.87	−9.58
A3	−10.19	−9.22
A4	−10.32	−9.58
A5	−11.25	−10.37
A6	−9.63	−8.96
Veliparib	−8.40	—
Colchicine	—	−10.07

Table 1 Computed global reactivity descriptors of the benzimidazolium compounds A1–A6

Compound	I (eV)	A (eV)	η (eV)	μ (eV)	χ (eV)	σ (eV^{-1})	ω (eV)	ξ
A1	9.43	4.78	2.33	−7.10	7.10	0.43	10.85	0.09
A2	9.28	4.76	2.26	−7.02	7.02	0.44	10.89	0.09
A3	9.39	4.76	2.31	−7.07	7.07	0.43	10.83	0.09
A4	9.36	4.75	2.30	−7.05	7.05	0.43	10.81	0.09
A5	9.14	4.71	2.21	−6.93	6.93	0.45	10.84	0.09
A6	8.61	4.72	1.94	−6.67	6.67	0.51	11.44	0.09

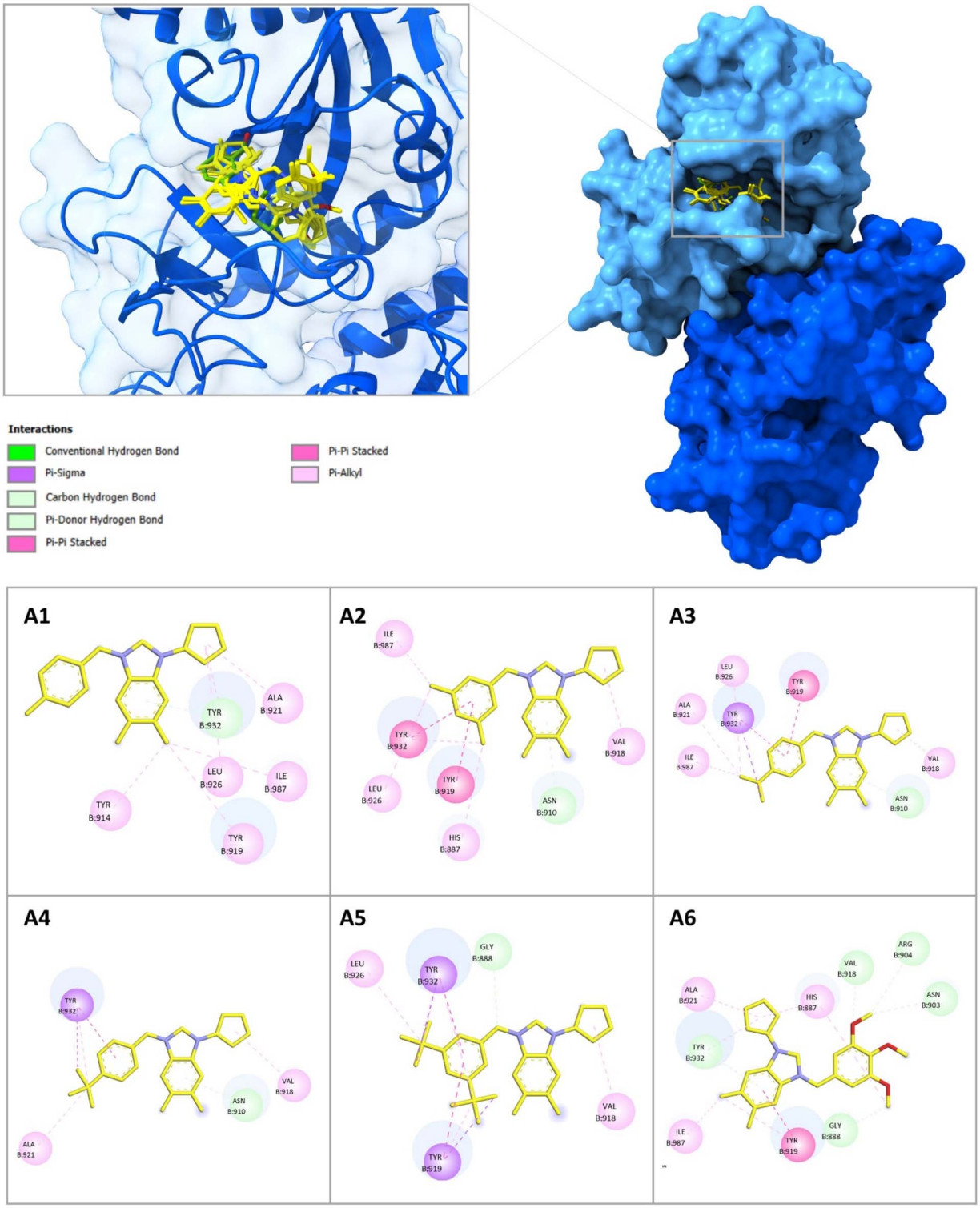

Fig. 5 Binding modes of benzimidazolium derivatives (**A1–A6**) within the active site of PARP-1 (PDB ID: 5LX6).

PARP-1 inhibition. Similarly, in the tubulin binding site, **A5** again demonstrates the most favorable binding energy (-10.37 kcal mol^{-1}), slightly stronger than that of colchicine (-10.07 kcal mol^{-1}). The outstanding binding affinity of **A5** can be attributed to the presence of two *tert*-butyl substituents at the 3,5-positions of the aromatic ring. These bulky, hydrophobic groups substantially increase the compound's nonpolar surface area, favoring hydrophobic and van der Waals interactions within the lipophilic pockets of both the PARP-1 and tubulin binding sites. The steric bulk of the *tert*-butyl groups may also

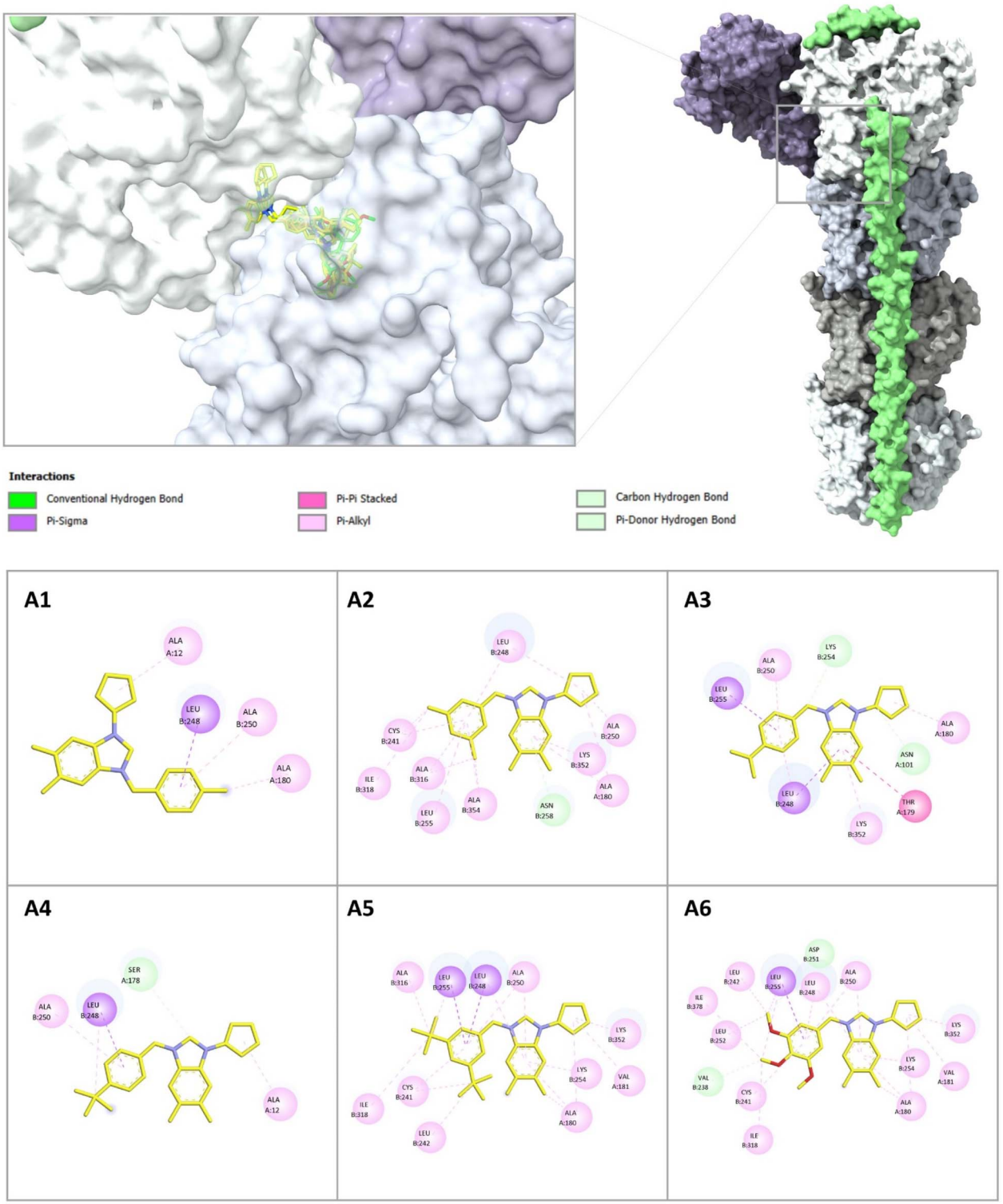

Fig. 6 Binding modes of benzimidazolium derivatives (**A1–A6**) within the tubulin binding site (PDB ID: 4O2B).

promote an optimal geometric complementarity with the binding cavity, thereby stabilizing the ligand–receptor complex. Importantly, this computational observation is consistent with the experimental results, where compound **A5** exhibited the highest cytotoxicity toward BEAS-2B cells and was among the most active derivatives against the SH-SY5Y cell line. Other compounds, particularly **A3** and **A4**, which also bear bulky substituents such as isopropyl and *tert*-butyl groups, exhibit binding affinities comparable to that of **A5**. This trend is in good agreement with the experimental findings, where these

derivatives also demonstrated notable cytotoxic activity, further supporting the positive influence of steric bulk on the interaction strength with these biological targets.

The interaction modes of the studied compounds within the active sites of the target enzymes are illustrated in Fig. 5 and 6. As shown in Fig. 5, all compounds primarily engage in hydrophobic interactions, with no significant hydrogen bonding observed. This finding is expected, as the benzimidazolium derivatives lack polar hydrogen atoms capable of forming hydrogen bonds. Compared with the native ligand veliparib (Fig. S1), most compounds interact with similar key residues within the PARP-1 binding pocket, notably TYR919, TYR932, GLY888, ALA921, and LEU926, indicating that they occupy the same active region of the enzyme. It is also noteworthy that the methyl groups of the bulky substituents participate in several hydrophobic contacts, further confirming the stabilizing role of these groups in enhancing the binding affinity and overall complex stability. A similar trend can be observed in Fig. 6, where most of the compounds interact with residues located in the same region as the colchicine–tubulin complex, indicating that they likely occupy a similar binding pocket. The interactions mainly involve residues such as LYS352, LEU255, and LEU248, which contribute to the stabilization of the ligand within the site. As in the case of PARP-1, the methyl groups of the bulky substituents play an important role in maintaining the stability of the complex through hydrophobic contacts.

Overall, the molecular docking results demonstrate that the benzimidazolium derivatives possess a strong ability to interact with both PARP-1 and tubulin, two key targets involved in cancer progression. Among the tested compounds, **A5** showed the most favorable binding energies toward both receptors, followed closely by **A3** and **A4**, reflecting the beneficial influence of bulky hydrophobic substituents on binding stability. The interaction analyses revealed that all compounds are mainly stabilized through hydrophobic contacts with key residues in the active sites. The good agreement between the computational findings and experimental cytotoxicity data further supports the reliability of the docking results and highlights **A5** as a promising lead structure for further optimization as a potential dual-target anticancer agent.

4. Conclusion

In this study, a series of novel benzimidazolium-based N-Heterocyclic Carbene (NHC) ligands and their corresponding selenium complexes were successfully synthesized and structurally confirmed using NMR, FT-IR, and mass spectrometry. The anticancer potential of these compounds was evaluated *in vitro* against colon (HCT116) and brain (SH-SY5Y) cancer cell lines, as well as a non-cancerous lung epithelial cell line (BEAS-2B), using the MTT assay. The results demonstrated that several ligands particularly **A3**, **A4**, and **A5** exhibited significantly higher cytotoxic activity than their selenium counterparts. These compounds showed lower IC_{50} values than the reference drug cisplatin, indicating strong potential as lead structures for further development. In contrast, the selenium complexes generally displayed weak or negligible activity across all tested cell lines. DFT and molecular docking studies further supported the *in vitro* findings by suggesting favorable interactions of the most active ligands with cancer-related protein targets. The ligands possess strong binding affinities toward PARP-1 and tubulin. Among them, compound **A5**, bearing bulky *tert*-butyl groups, demonstrated the best docking scores and experimental cytotoxicity, highlighting the beneficial role of hydrophobic substituents in enhancing biological interactions. These results highlight the critical role of ligand structure in determining bioactivity and suggest that future modifications should focus on optimizing the benzimidazolium core rather than relying on selenium coordination. Overall, this work contributes to the understanding of structure–activity relationships in NHC-based compounds, the work demonstrates that benzimidazolium salts, rather than their selenium adducts, hold greater promise as anticancer scaffolds and provides a promising foundation for the development of new NHC-based agents with optimized reactivity and target selectivity.

Conflicts of interest

The author has no conflicts of interest to declare.

Data availability

The data supporting this article have been included as part of the supplementary information (SI). Supplementary information is available. See DOI: https://doi.org/10.1039/d5ra08393a.

Acknowledgements

The authors greatly acknowledge financial support from the İnönü University Research Fund (Project No: FBA-2025-4374) for this work. The supercomputing resources used in this work were supported by the HPC of UCI-UFMC (Unité de Calcul Intesif of the University Fréres Mentouri Constantine 1).

References

1 B. Rosenberg, L. Van Camp and T. Krigas, Inhibition of cell division in Escherichia coli by electrolysis products from a platinum electrode, *Nature*, 1965, **205**, 698–699.
2 C. A. Rabik and M. E. Dolan, Molecular mechanisms of resistance and toxicity associated with platinating agents, *Cancer Treat Rev.*, 2007, **33**, 9–23.
3 V. M. Miranda, Medicinal inorganic chemistry: An updated review on the status of metallodrugs and prominent metallodrug candidates, *Rev. Inorg. Chem.*, 2022, **42**, 29–52.
4 B. Bertrand and A. Casini, A golden future in medicinal inorganic chemistry: the promise of anticancer gold organometallic compounds, *Dalton Trans.*, 2014, **43**, 4209–4219.
5 A. R. M. Sikkander, M. Meena, H. Yadav, N. Wahi and V. V. Lakshmi, Appraisal of the impact of applying organometallic compounds in cancer therapy, *J. Appl. Organomet. Chem.*, 2024, **4**, 145–166.

6 E. M. Nagy, L. Ronconi, C. Nardon and D. Fregona, Noble metal-dithiocarbamates precious allies in the fight against cancer, *Mini Rev. Med. Chem.*, 2012, **12**, 1216–1229.
7 L. Ronconi and P. J. Sadler, Using coordination chemistry to design new medicines, *Coord. Chem. Rev.*, 2007, **251**, 1633–1648.
8 T. J. Siciliano, M. C. Deblock, K. M. Hindi, S. Durmus, M. J. Panzner, C. A. Tessier and W. J. Youngs, Synthesis and anticancer properties of gold(I) and silver(I) N-heterocyclic carbene complexes, *J. Organomet. Chem.*, 2011, **696**, 1066–1071.
9 G. Sava, A. Bergamo and P. J. Dyson, Metal-based antitumour drugs in the post-genomic era: what comes next?, *Dalton Trans.*, 2011, **40**, 9069–9075.
10 B. Boualia, A. el-K. Sandeli, H. Boulebd, H. Karci, M. Dundar, İ. Özdemir, N. Gürbüz, A. Koç, R. Menacer and İ. Özdemir, Exploring the antimicrobial potential of new selenium-N-heterocyclic carbene complexes and their benzimidazolium salts: synthesis, characterization, biological evaluation, and docking insights, *Chem. Pap.*, 2025, **79**, 1439–1454.
11 N. Iqbal, M. Yaqoob, M. Javed, M. Abbasi, J. Iqbal and M. A. Iqbal, Synthesis in combination with biological and computational evaluations of selenium-N-heterocyclic carbene compounds, *Comput. Theor. Chem.*, 2021, **1197**, 113135.
12 S. P. Nolan, *N-heterocyclic Carbenes in Synthesis*, John Wiley & Sons, 2006.
13 C. D. Campbell, K. B. Ling and A. D. Smith, N-Heterocyclic carbenes in organocatalysis, in *N-heterocyclic Carbenes in Transition Metal Catalysis and Organocatalysis*, Springer, 2010, pp. 263–297.
14 N. Y. Rusetskaya, I. V. Fedotov, V. A. Koftina and V. B. Borodulin, Selenium compounds in redox regulation of inflammation and apoptosis, Biochemistry Moscow, Supplement Series B, *Biomed. Chem.*, 2019, **13**, 277–292.
15 Y. Saito, Essential trace element selenium and redox regulation: its metabolism, physiological function, and related diseases, *Redox Exp. Med.*, 2022, R149–R158.
16 N. Iqbal, M. Yaqoob, M. Javed, M. Abbasi, J. Iqbal and M. A. Iqbal, Synthesis in combination with biological and computational evaluations of selenium-N-heterocyclic carbene compounds, *Comput. Theor. Chem.*, 2021, **1197**, 113135.
17 A. el-K. Sandeli, N. Khiri-Meribout, S. Benzerka, H. Boulebd, N. Gürbüz, N. Özdemir and İ. Özdemir, Synthesis, structures, DFT calculations, and catalytic application in the direct arylation of five-membered heteroarenes with aryl bromides of novel palladium-N-heterocyclic carbene PEPPSI-type complexes, *New J. Chem.*, 2021, **45**, 17878–17892.
18 A. E.-K. Sandeli, N. Khiri-Meribout, S. Benzerka, N. Gürbüz, M. Dündar, H. Karcı, C. Bensouici, E. H. Mokrani, İ. Özdemir and A. Koc, Silver(I)-N-heterocyclic carbene complexes: Synthesis and characterization, biological evaluation of anti-cholinesterase, anti-alpha-amylase, anti-lipase, and antibacterial activities, and molecular docking study, *Inorg. Chim. Acta*, 2021, **525**, 120486.
19 T. J. Siciliano, M. C. Deblock, K. M. Hindi, S. Durmus, M. J. Panzner, C. A. Tessier and W. J. Youngs, Synthesis and anticancer properties of gold(I) and silver(I) N-heterocyclic carbene complexes, *J. Organomet. Chem.*, 2011, **696**, 1066–1071.
20 A. el-K. Sandeli, N. Khiri-Meribout, S. Benzerka, H. Boulebd, N. Gürbüz, N. Özdemir and İ. Özdemir, Synthesis, structures, DFT calculations, and catalytic application in the direct arylation of five-membered heteroarenes with aryl bromides of novel palladium-N-heterocyclic carbene PEPPSI-type complexes, *New J. Chem.*, 2021, **45**, 17878–17892.
21 A. E.-K. Sandeli, H. Boulebd, N. Khiri-Meribout, S. Benzerka, C. Bensouici, N. Özdemir, N. Gürbüz and İ. Özdemir, New benzimidazolium N-heterocyclic carbene precursors and their related Pd-NHC complex PEPPSI-type: Synthesis, structures, DFT calculations, biological activity, docking study, and catalytic application in the direct arylation, *J. Mol. Struct.*, 2022, **1248**, 131504.
22 J. C. Garrison and W. J. Youngs, Ag(I) N-heterocyclic carbene complexes: synthesis, structure, and application, *Chem. Rev.*, 2005, **105**, 3978–4008.
23 F. Tian, Y. Chen, P. Li and S. Lu, A novel method for synthesis of 1,3-dialkylimidazole-2-selenones in water, *Phosphorus Sulfur Silicon Relat. Elem.*, 2014, **189**, 1391–1395.
24 M. A. Iqbal, R. A. Haque, W. C. Ng, L. E. H. Hassan, A. M. S. A. Majid and M. R. Razali, Green synthesis of mono- and di-selenium-N-heterocyclic carbene adducts: Characterizations, crystal structures and pro-apoptotic activities against human colorectal cancer, *J. Organomet. Chem.*, 2016, **801**, 130–138.
25 N. Sharma, G. Arya, R. M. Kumari, N. Gupta and S. Nimesh, Evaluation of anticancer activity of silver nanoparticles on the A549 human lung carcinoma cell lines through alamar blue assay, *Bio-Protoc.*, 2019, **9**, e3131.
26 M. Frisch *et al*, *Gaussian 09, Revision D.01*, Gaussian, Inc., Wallingford CT, 2009, vol. 201.
27 T. Lu and F. Chen, Multiwfn: A multifunctional wavefunction analyzer, *J. Comput. Chem.*, 2012, **33**, 580–592.
28 W. Humphrey, A. Dalke and K. Schulten, VMD: Visual molecular dynamics, *J. Mol. Graphics*, 1996, **14**, 33–38.
29 G. M. Morris, R. Huey, W. Lindstrom, M. F. Sanner, R. K. Belew, D. S. Goodsell and A. J. Olson, AutoDock4 and AutoDockTools4: Automated docking with selective receptor flexibility, *J. Comput. Chem.*, 2009, **30**, 2785–2791.
30 J. Eberhardt, D. Santos-Martins, A. F. Tillack and S. Forli, AutoDock Vina 1.2.0: New docking methods, expanded force field, and python bindings, *J. Chem. Inf. Model.*, 2021, **61**, 3891–3898.
31 G. Steiner, H. Kopacka, K. Ongania, K. Wurst, P. Preishuber-Pflügl and B. Bildstein, Heteroditopic imino N-heterocyclic carbenes and their sulfur, selenium, and tungsten tetracarbonyl derivatives, *Eur. J. Inorg. Chem.*, 2005, **2005**, 1325–1333.
32 P. S. Engl, R. Senn, E. Otth and A. Togni, Synthesis and characterization of N-trifluoromethyl N-heterocyclic

carbene ligands and their complexes, *Organometallics*, 2015, **34**, 1384–1395.

33 T. J. Siciliano, M. C. Deblock, K. M. Hindi, S. Durmus, M. J. Panzner, C. A. Tessier and W. J. Youngs, Synthesis and anticancer properties of gold(I) and silver(I) N-heterocyclic carbene complexes, *J. Organomet. Chem.*, 2011, **696**, 1066–1071.

34 M. A. Iqbal, R. A. Haque, W. C. Ng, L. E. H. Hassan, A. M. S. A. Majid and M. R. Razali, Green synthesis of mono- and di-selenium-N-heterocyclic carbene adducts: Characterizations, crystal structures and pro-apoptotic activities against human colorectal cancer, *J. Organomet. Chem.*, 2016, **801**, 130–138.

35 R. A. Haque, M. A. Iqbal, F. Mohamad and M. R. Razali, Antibacterial and DNA cleavage activity of carbonyl functionalized N-heterocyclic carbene-silver(I) and selenium compounds, *J. Mol. Struct.*, 2018, **1155**, 362–370.

36 A. Kamal, V. M. Nazari, M. Yaseen, M. A. Iqbal, M. B. K. Ahamed, A. S. A. Majid and H. N. Bhatti, Green synthesis of selenium-N-heterocyclic carbene compounds: Evaluation of antimicrobial and anticancer potential, *Bioorg. Chem.*, 2019, **90**, 103042.

37 H. Boulebd, A comprehensive DFT-based study of the antioxidant properties of monolignols: Mechanism, kinetics, and influence of physiological environments, *Int. J. Biol. Macromol.*, 2025, **284**, 138044.

38 F. Montecinos, M. Loew, T. I. Chio, S. L. Bane and D. L. Sackett, Interaction of colchicine-site ligands with the blood cell-specific isotype of β-tubulin—notable affinity for benzimidazoles, *Front. Cell Dev. Biol.*, 2022, **10**, 884287.

39 A. Beč, L. Hok, L. Persoons, E. Vanstreels, D. Daelemans, R. Vianello and M. Hranjec, Synthesis, computational analysis, and antiproliferative activity of novel benzimidazole acrylonitriles as tubulin polymerization inhibitors: Part 2, *Pharmaceuticals*, 2021, **14**, 1052.

40 T.-T. Miao, X.-B. Tao, D.-D. Li, H. Chen, X.-Y. Jin, Y. Geng, S.-F. Wang and W. Gu, Synthesis and biological evaluation of 2-aryl-benzimidazole derivatives of dehydroabietic acid as novel tubulin polymerization inhibitors, *RSC Adv.*, 2018, **8**, 17511–17526.

41 T. D. Penning, G.-D. Zhu, V. B. Gandhi, J. Gong, X. Liu, Y. Shi, V. Klinghofer, E. F. Johnson, C. K. Donawho and D. J. Frost, Discovery of the poly(ADP-ribose) polymerase (PARP) inhibitor 2-[(R)-2-methylpyrrolidin-2-yl]-1H-benzimidazole-4-carboxamide (ABT-888) for the treatment of cancer, *J. Med. Chem.*, 2009, **52**, 514–523.

42 C. K. Donawho, Y. Luo, Y. Luo, T. D. Penning, J. L. Bauch, J. J. Bouska, V. D. Bontcheva-Diaz, B. F. Cox, T. L. DeWeese and L. E. Dillehay, ABT-888, an orally active poly(ADP-ribose) polymerase inhibitor that potentiates DNA-damaging agents in preclinical tumor models, *Clin. Cancer Res.*, 2007, **13**, 2728–2737.